The Astrophysical Journal, 666:806–816, 2007 September 10

SPITZER QUASAR AND ULIRG EVOLUTION STUDY (QUEST). II. THE SPECTRAL ENERGY DISTRIBUTIONS OF PALOMAR-GREEN QUASARS

Hagai Netzer,[1] Dieter Lutz,[2] Mario Schweitzer,[2] Alessandra Contursi,[2] Eckhard Sturm,[2] Linda J. Tacconi,[2] Sylvain Veilleux,[3] D.-C. Kim,[3] David Rupke,[3] Andrew J. Baker,[4] Kalliopi Dasyra,[5] Joseph Mazzarella,[5] and Steven Lord[6]

Received 2007 March 7; accepted 2007 June 4

ABSTRACT

This is the second paper studying the QSOs in the *Spitzer* QUEST sample. Previously we presented new PAH measurements and argued that most of the observed far-infrared (FIR) radiation is due to star-forming activity. Here we present spectral energy distributions (SEDs) by supplementing our data with optical, NIR, and FIR observations. We define two subgroups, of "weak FIR" and "strong FIR" QSOs, and a third group of FIR nondetections. Assuming a starburst origin for the FIR, we obtain "intrinsic" active galactic nucleus (AGN) SEDs by subtracting a starburst template from the mean SEDs. The resulting SEDs are remarkably similar for all groups. They show three distinct peaks corresponding to two silicate emission features and a 3 μm bump, which we interpret as the signature of the hottest AGN dust. They also display drops beyond $\sim$20 μm that we interpret as the signature of the minimum temperature ($\sim$200 K) dust. This component must be optically thin to explain the silicate emission and the slope of the long-wavelength continuum. We discuss the merits of an alternative model in which most of the FIR emission is due to AGN heating. Such models are unlikely to explain the properties of our QSOs, but they cannot be ruled out for more luminous objects. We also find correlations between the luminosity at 5100 Å and two infrared starburst indicators: L(60 μm) and L(PAH 7.7 μm). The correlation of L(5100 Å) with L(60 μm) can be used to measure the relative growth rates and lifetimes of the black hole and the new stars.

Subject headings: galaxies: active — galaxies: starburst — infrared: galaxies — quasars: emission lines

Online material: machine-readable table

1. INTRODUCTION

The spectral energy distributions (SEDs) of active galactic nuclei (AGNs) have been studied extensively over various energy bands and for different subgroups of the AGN population (e.g., Sanders et al. 1989; Elvis et al. 1994; Scott et al. 2004; Haas et al. 2003; Glikman et al. 2006; Richards et al. 2006, hereafter R06; Trammell et al. 2007). Such studies are essential for estimating the bolometric luminosities of AGNs, for distinguishing between the various subclasses, and for deriving the relationships between black hole (BH) mass, luminosity, and accretion rate. They are also required for understanding the details of the energy production mechanisms at X-ray, UV, optical, infrared (IR), and radio energies. The shape of the observed SED depends on the BH mass and accretion rate, the structure and inclination of the central accretion disk, the presence and the geometry of a dusty central structure, the line-of-sight absorption and extinction, the presence of luminous starburst regions in the host galaxy, and the properties of any central radio source.

The various SED bands can be classified according to the origin of the emitted energy. Here we define "primary radiation" as the part produced within the inner 1000 gravitational radii (to include the entire central accretion disk). "Secondary radiation" is the energy emitted outside of this radius, due to absorption and reprocessing of primary radiation. The term "intrinsic radiation" is used to define everything associated with the AGN, i.e., the primary radiation as well as radiation from the vicinity of the BH due to the reprocessing of the primary radiation.

Dust in the immediate vicinity of the central source is known to be a major source of secondary radiation and is probably responsible for most of the emergent near-infrared (NIR) and mid-infrared (MIR) continuum. The amount intrinsic AGN-heated dust emission contributes to the far-infrared (FIR) emission spectrum has been an open question for years. This issue was discussed extensively in our first paper (Schweitzer et al. 2006, hereafter Paper I), where many relevant references are listed, and it is also a major topic of the present work. It is directly related to the possible contribution of star-forming (SF) regions to the FIR emission and the maximum and minimum temperatures of the AGN-heated dust.

Most previous studies of AGN SEDs in the MIR, especially those focusing on the more luminous AGNs, were limited by the sensitivity and resolution of earlier MIR instrumentation. This circumstance is now changing, as new *Spitzer* observations are capable of providing high-quality data on larger AGN samples. For example, Lacy et al. (2004) found that detection methods based on MIR colors are efficient tools for selecting all types of AGNs (and also starburst galaxies). The addition of optical colors makes such methods even more efficient (R06). Combinations of optical-MIR colors have been used by Hatziminaoglou et al. (2005) to derive mean type I SEDs and to investigate the distribution of the bolometric luminosity in small AGN samples. R06 used a much larger sample of 259 Sloan Digital Sky Survey

[1] School of Physics and Astronomy, and the Wise Observatory, Raymond and Beverly Sackler Faculty of Exact Sciences, Tel-Aviv University, Tel-Aviv 69978, Israel.
[2] Max-Planck-Institut für extraterrestrische Physik, 85741 Garching, Germany.
[3] Department of Astronomy, University of Maryland, College Park, MD 20742-2421.
[4] Department of Physics and Astronomy, Rutgers University, Piscataway, NJ 08854-8019.
[5] Spitzer Science Center, California Institute of Technology, Pasadena CA 91125.
[6] NASA Herschel Science Center, California Institute of Technology, Pasadena CA 91125.

(SDSS) sources, as well as an optical-MIR color combination, to illustrate the diversity of AGN SEDs and to study the bolometric luminosity and accretion rates in such sources.

The present work is a continuation of our study of the QUEST sample, which is described in detail in Paper I. In brief, we are studying QSOs, ultraluminous infrared galaxies (ULIRGs), and the possible evolutionary connection between the two using data from the *Spitzer* Infrared Spectrograph (IRS). The QSO sample is largely drawn from that of Guyon et al. (2006). It consists of Palomar-Green (PG) QSOs and covers the full ranges of bolometric luminosity ($10^{11.5}$–10^{13} $L_\odot$), radio loudness, and infrared excess [$\nu L_\nu(60\ \mu\mathrm{m})/L_{\mathrm{bol}} \sim 0.02$–$0.35$] spanned by the local members of the PG QSO sample. The ULIRGs in the sample will be described in detail in a forthcoming publication.

Unlike the SED studies mentioned above, we use detailed *Spitzer* spectroscopy, which allows us to expand on the earlier broadband work. A major goal of this study is to use MIR spectroscopy in combination with broadband FIR photometry in an attempt to investigate the origin of the FIR emission in intermediate-luminosity QSOs. Such objects are classified by R06 as "normal type 1 quasars." In Paper I we focused on PAH features and the correlation of their luminosity with the FIR luminosity of the sources. We detected clear PAH emission in 11 of our sources and argued for its likely presence in most other QSOs. We then used known relationships between PAH emission and star-forming activity, as well as the great similarity of $L(\mathrm{PAH}\ 7.7\ \mu\mathrm{m})/L(60\ \mu\mathrm{m})$ in QUEST QSOs and the starburst-dominated objects among the QUEST ULIRGs, to argue that at least a third and perhaps all of the 50–100 μm luminosity in our QSO sample is due to star formation. Here we present the entire 1–100 μm SED of the QUEST QSOs and use the continuum properties to further investigate the PAH emission as well as other observed MIR features. A major goal is to identify the "pure" or "intrinsic" AGN SED that is produced entirely by the central AGN, with no starburst contamination.

Section 2 of the paper presents the MIR continuum spectra of the QSOs in our sample and shows derived SEDs for two subgroups with weak and strong detected FIR emission, as well as for FIR nondetections. In § 3 we introduce the intrinsic AGN-powered SED and discuss the implications for AGN models and the AGN-starburst connection.

2. THE INFRARED SED OF QUEST QSOs

2.1. *Spitzer Spectra*

Our reduction and analysis procedure is described in Paper I. The original QUEST sample includes 25 AGNs plus 4 others with similar properties (I Zw 1, PG 1244+026, PG 1448+273, and Mrk 1014) that were added from other samples. The data presented here include two QSOs (PG 0844+349 and PG 0923+201) that were not included in Paper I because of their later observation dates. The combined sample now includes a total of 29 QSOs. We use the flux-calibrated 6–35 μm spectra and convert them to monochromatic luminosity (L_λ ergs s^{-1} Å^{-1}) using a standard cosmology with $H_0 = 70$ km s^{-1} Mpc^{-1}, $\Omega_m = 0.3$, and $\Omega_\Lambda = 0.7$. Figure 1 shows the *Spitzer* spectra of these QSOs, while the main spectral lines and features are identified in Figure 2. The spectra are shifted in luminosity to avoid crowding and allow an easier intercomparison of the overall spectral shape. They are also deredshifted to compare features in the same reference frame. As clearly seen in this diagram, and in several of the diagrams shown in Paper I, there is a large variety of spectral shapes: some objects show a clear increase of λL_λ with λ, while in others there is a definite change of slope and a clear decline for $\lambda > 15$ μm. $L(60\ \mu\mathrm{m})/L(15\ \mu\mathrm{m})$, a useful measure of the FIR/MIR luminosity ratio, varies by up to a factor of 10 in our sample. The luminosity range in our sample is a factor of about 100 in $L(15\ \mu\mathrm{m})$ and does not represent the entire type I AGN population, since very high luminosity sources are missing from the sample. Thus, we are not in a position to investigate as large a range of SED properties as the one studied, for example, in R06. As noted in Paper I, most and perhaps all sources show signatures of silicate emissions peaking at around 10 and around 18 μm. These features are the subject of a forthcoming paper.

In what follows we purposely avoid discussing sharp spectral features such as emission lines. These will be discussed in a separate paper. All spectra shown below are presented on a rest wavelength scale to allow easier comparison among sources. For one of the targets shown in Figure 1 (PG 1307+085), the low-resolution IRS data down to 5 μm are still proprietary to another program. This source is excluded from much of the subsequent analysis.

2.2. *NIR and FIR Data*

The basic *Spitzer* data and the FIR data obtained from the literature for all but two recently observed sources are given in Paper I (Table 1). We have supplemented these with NIR data and FIR data for the two new sources obtained from the literature. The NIR data were obtained from various sources, in particular Neugebauer et al. (1987) and the 2MASS extended and point source catalogs (Jarrett et al. 2000). Table 1 lists the adopted *JHKL* fluxes and references, where available. We have also added the optical luminosity at 5100 Å, obtained from the original data of Boroson & Green (1992) and kindly supplied by T. Boroson (2006, private communication). As discussed below, this makes an important connection to the primary SED of the sources. Variability may in principle affect the SEDs, since many of the optical/near-infrared data were taken about 20 years before the *Spitzer* observations. As for the new FIR data, we followed the procedure in Paper I and obtained the luminosity at 60 μm rest wavelength by interpolating the observed fluxes at 60 and 100 μm. $L(60\ \mu\mathrm{m})$ is very similar to the standard $L(\mathrm{FIR})$ used extensively in the literature, but it is relatively robust to cirrus contamination at 100 μm for these faint sources. The FIR luminosities computed this way for the two sources not included in Paper I are $10^{10.38}$ $L_\odot$ (PG 0844+349) and $<10^{11.90}$ $L_\odot$ (PG 0923+201). Hereafter we assume $L(\mathrm{FIR}) = L(60\ \mu\mathrm{m})$.

We extend the IRS spectra to shorter and longer wavelengths by spline interpolations using the photometry obtained from the literature. The dominant sources of uncertainty in this procedure are the photometric uncertainties on the data collected from the literature and the possible continuum variations at short wavelengths, since we are using nonsimultaneous observations (see also Fig. 4). We also compared our data with the recent Glikman et al. (2006) composite obtained from a sample of 27 AGNs that cover a redshift and luminosity range similar to the QUEST QSOs. Their composite is of higher quality at shorter wavelength, and it is shown next to our composite SED in Figure 3.

2.3. *Strong, Weak, and Nondetected Far-Infrared Sources*

To represent the range of FIR properties in our sample, we divide the QSOs with FIR detections into strong FIR and weak FIR emitters, with a dividing line at rest $L(60\ \mu\mathrm{m})/L(15\ \mu\mathrm{m}) = 1$. Our definition thus implies "strong" or "weak" with respect to the mid-IR, emission rather than in an absolute sense. Out of the 21 QSOs in our sample with detectable FIR flux, two (PG 2214+139 and PG 1626+554) are problematic, since the *Spitzer* spectra

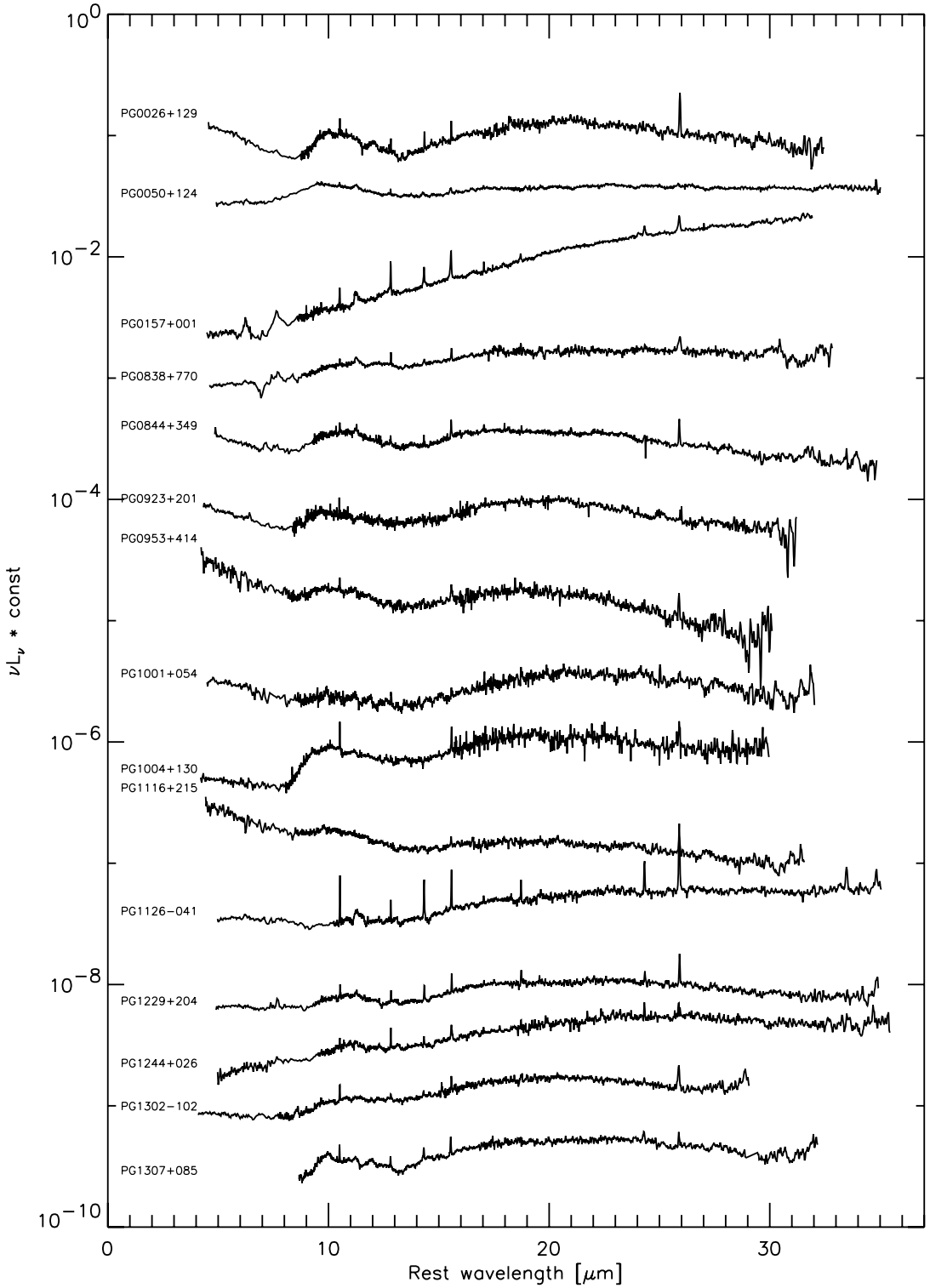

FIG. 1.—IRS spectra of QUEST QSOs deredshifted to rest-frame wavelengths and given in νL_ν units. The spectra are shifted vertically to allow a clearer view. See Fig. 2 for identification of the main spectral features.

show a clear decline of λL_λ, from 15 to 30 μm, yet the $L(60\ \mu\mathrm{m})$ point lies clearly above the extrapolation of this spectrum. We suspect that the large-aperture FIR data, close to the detection flux limit of the *IRAS* and *ISO* instruments, are error prone, so we have chosen to leave those sources out of the analysis. Also excluding PG 1307+085, there remain 18 high-quality SEDs extending to the FIR, out of which 10 are classified as strong FIR sources and 8 as weak FIR sources. The remaining 8 sources without FIR detection define a third subsample; as explained in Paper I, these are more likely to belong to the class of weak FIR emitters and to also show very low equivalent width PAH 7.7 μm emission, rather than having a rising IR flux but a long-wavelength flux below the detection limit. We include the IRS and short-wavelength data of those targets where applicable.

Figure 3 shows the mean SEDs of the full sample (excluding PG 1307+085) as well as of the above three FIR subgroups. The

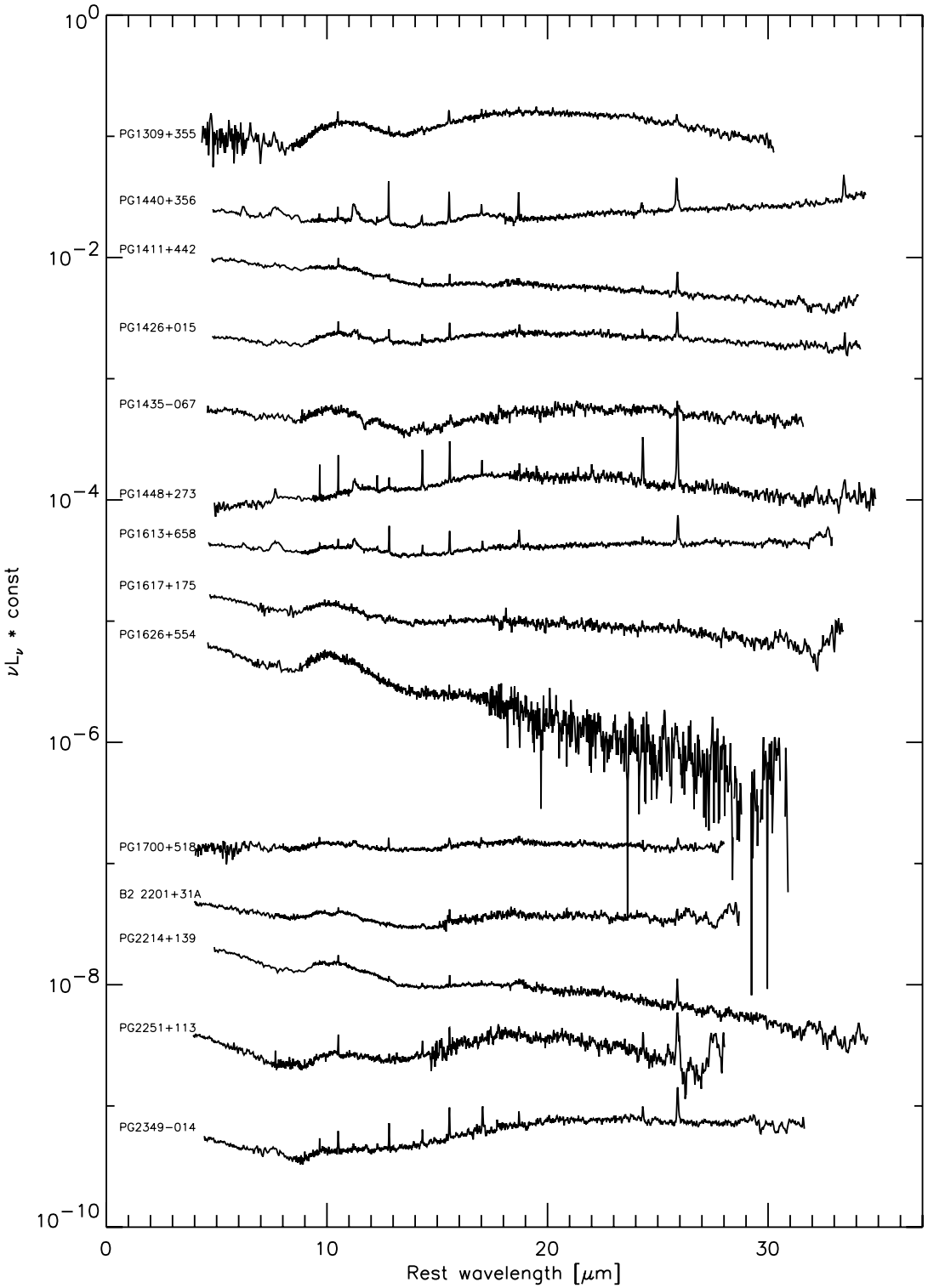

FIG. 1—*Continued*

relative fluxes of the full SED are given in Table 2. Setting aside emission lines and PAH features, all these mid-infrared SEDs show three pronounced peaks: one at 2–3 μm plus the two silicate peaks at $\sim$10 and $\sim$18 μm. In addition to these components, there is a differing amount of FIR emission according to the specific subgroup. As discussed in Paper I, FIR emission and PAH emission from the hosts of PG QSOs are correlated. Indeed, Figure 3 shows that the equivalent width of PAH 7.7 μm varies along with the far-infrared properties of the three subgroups.

The scatter of SED shapes within each group is indicated in Figure 4. The SEDs clearly show upturns and downturns at long wavelengths ($\lambda > 40$ μm), justifying the terms strong and weak FIR sources. However, there is a range of properties within each group and a continuous transition from one to the other. We also show the three mean SEDs (*thick black lines*). We prefer the use

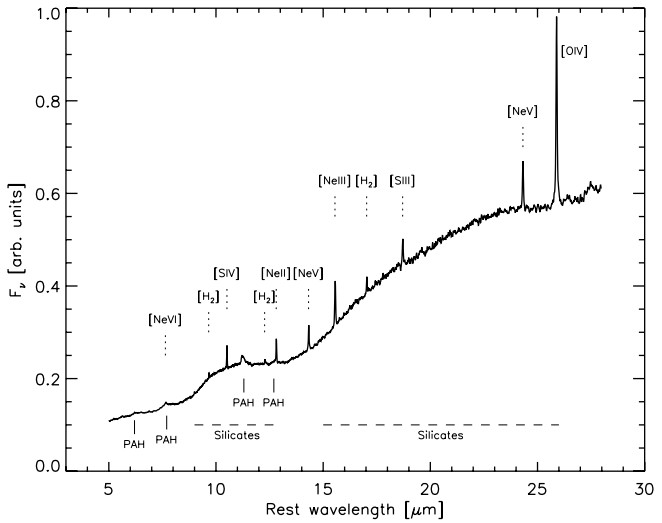

FIG. 2.—Average IRS spectrum of all QSOs except PG 1307+085. The main emission lines and features are marked.

of mean rather than median spectra because they better preserve the integrity of features in the SEDs and because of the small number of sources. However, the overall differences between the median and the mean SEDs are not large.

The individual source SEDs sometimes show structure at $\lambda < 5$ μm, which may be due to uncertain (literature) photometry and/or variability. However, the detections of the three peaks noted above in all mean SEDs of Figure 3 suggest this result is robust.

The results shown here are consistent with the conclusions of Paper I, that most and perhaps all QSOs show some level of PAH emission and that any classifications into PAH-detected and non–PAH-detected categories are likely due to a combination of real differences in EW(PAH 7.7 μm) (or other PAHs) and observational limitations (e.g., aperture affects). It is therefore not surprising that both groups, of strong and weak FIR sources, include sources with detectable PAH 7.7 μm. We expect future higher signal-to-noise ratio spectra to reveal currently nondetected PAHs. In summary, the observations of the QUEST QSOs suggest that we are sampling a distribution in all three properties: PAH luminosity, FIR luminosity, and SED shape, with a tendency for larger FIR luminosity sources to have larger L(PAH 7.7 μm) and a long-wavelength upturn of their SED.

TABLE 1
QSO SAMPLE AND SUPPLEMENTARY DATA

Object (1)	z (2)	log L_{5100} (ergs s^{-1}) (3)	S_J (mJy) (4)	S_H mJy (5)	S_K (mJy) (6)	S_L (mJy) (7)	References (8)	FIR Class (for plot) (9)
PG 0026+129	0.1420	44.66	4.47	5.82	8.51	17.99	N87	Undetected
PG 0050+124 (IZw 1)	0.0611	44.30	21.30	34.40	55.70	127.00	2M, S89	Strong
PG 0157+001 (Mrk 1014)	0.1630	44.67	6.06	7.99	12.70	17.38	2M, N87	Strong
PG 0838+770	0.1310	44.16	2.29	3.09	4.79	6.31	N87	Weak
PG 0844+349	0.0640	44.00	6.03	8.51	13.18	23.99	N87	Weak
PG 0923+201	0.1900	44.89	2.90	4.52	8.79	14.70	2M, S89	Undetected
PG 0953+414	0.2341	45.11	3.39	4.27	7.76	15.49	N87	Undetected
PG 1001+054	0.1605	44.25	1.47	2.21	4.10	...	H82	Strong
PG 1004+130	0.2400	45.23	4.17	4.27	5.82	9.12	N87	Weak
PG 1116+215	0.1765	45.13	5.83	8.64	16.15	32.50	2M, S89	Undetected
PG 1126−041 (Mrk 1298)	0.0600	43.82	11.20	16.90	25.00	24.70	2M,S89	Strong
PG 1229+204 (Mrk 771)	0.0630	44.13	6.03	8.51	13.18	23.99	N87	Weak
PG 1244+026	0.0482	43.26	2.84	3.66	4.79	...	2M	Strong
PG 1302−102	0.2784	45.17	3.36	3.77	4.89	...	H82	Strong
PG 1307+085	0.1550	44.87	3.55	4.32	6.92	10.32	N87	Weak
PG 1309+355	0.1840	44.81	3.33	3.63	5.76	...	2M	Undetected
PG 1411+442	0.0896	44.31	5.62	8.32	17.38	38.91	N87	Weak
PG 1426+015	0.0865	44.44	5.89	8.71	15.85	23.44	N87	Weak
PG 1435−067	0.1260	44.39	2.52	3.23	5.84	...	2M	Strong
PG 1440+356 (Mrk 478)	0.0791	44.22	9.77	15.14	25.12	38.91	N87	Strong
PG 1448+273	0.0650	43.99	6.17	8.41	11.89	15.14	N87	Weak
PG 1613+658 (Mrk 876)	0.1290	44.70	4.57	6.31	10.72	17.38	N87	Strong
PG 1617+175	0.1124	44.29	4.27	6.46	12.30	19.50	N87	Undetected
PG 1626+554	0.1330	44.44	2.75	3.43	5.68	...	2M	?
PG 1700+518	0.2920	45.68	4.37	6.53	12.74	30.90	N87	Weak
B2 2201+31A	0.2950	45.91	2.61	4.24	7.73	...	2M	Undetected
PG 2214+139 (Mrk 304)	0.0658	44.40	12.20	16.30	22.90	26.30	2M, M83	?
PG 2251+113	0.3255	45.63	3.39	4.68	7.24	10.72	N87	Undetected
PG 2349−014	0.1740	45.21	4.17	5.57	9.55	17.78	N87	Strong

NOTES.—Col. (1): Source name. Col. (2): Redshift. Cols. (3): Continuum luminosity λL_λ at 5100 Å rest wavelength (from spectra by T. Boroson 2006, private communication). Cols. (4–8): Near-infrared fluxes in the *JHKL* observed bands, and related references: 2M: 2MASS magnitudes, extended source catalog (Jarrett et al. 2000); K20 isophotal magnitudes for slightly extended sources, point source catalog magnitudes otherwise; H82: Hyland & Allen (1982); M83: McAlary et al. (1983); N87: Neugebauer et al. (1987); S89: Sanders et al. (1989). Col. (9): Classification as far-infrared strong/weak (relative to the mid-infrared), or undetected. See text for definition and treatment of PG 1626+554 and PG 2214+139.

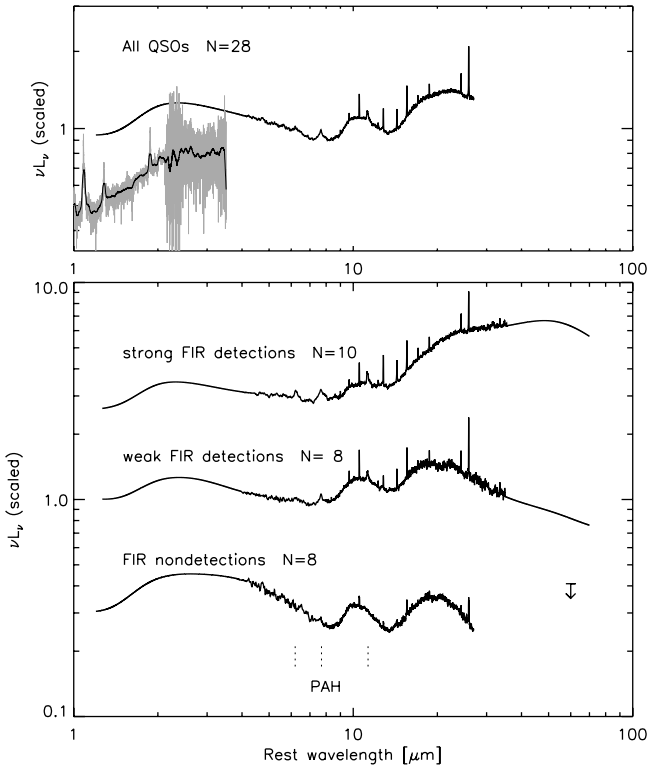

FIG. 3.—*Top*: Average SEDs for QUEST QSOs in our sample, normalized at 6 μm. For comparison, we overplot the mean SED derived from ground-based data at shorter wavelengths for a QSO sample of similar luminosity by Glikman et al. (2006) shifted by an arbitrary amount. *Bottom*: Average SEDs for the three subgroups of strong FIR detections, weak FIR detections, and FIR nondetections. Note the increase of EW(PAH 7.7 μm) from bottom to top.

2.4. *Correlations between L(FIR) and L(PAH) and the Primary AGN Luminosity*

So far we have only considered the NIR, MIR, and FIR parts of the SED. These are mostly due to thermal emission from cool and hot dust, both of which by definition are secondary sources of radiation. Our data set also includes the 4000–6000 Å spectra

TABLE 2
AVERAGE QSO SEDs

Rest Wavelength (μm) (1)	Observed QSO SED λF_λ (arbitrary units) (2)	Intrinsic AGN SED for FIR-weak QSOs λF_λ (arbitrary units) (3)
1.202	0.944	0.974
1.216	0.944	0.973
1.230	0.945	0.972
1.245	0.946	0.972
1.259	0.947	0.971
1.274	0.948	0.971
1.288	0.949	0.971
1.303	0.951	0.971
1.318	0.953	0.971
1.334	0.956	0.972
1.349	0.959	0.973

NOTES.—Table 2 is published in its entirety in the electronic edition of the *Astrophysical Journal*. A portion is shown here for guidance regarding its form and content. Col. (1): Rest wavelength. Col. (2): Average observed SED of 28 PG QSOs (see Fig. 3, *top*, smoothed). Col. (3): Average intrinsic AGN SED of 8 FIR-weak PG QSOs, after subtraction of a starburst component (see Fig. 6, *right*, smoothed).

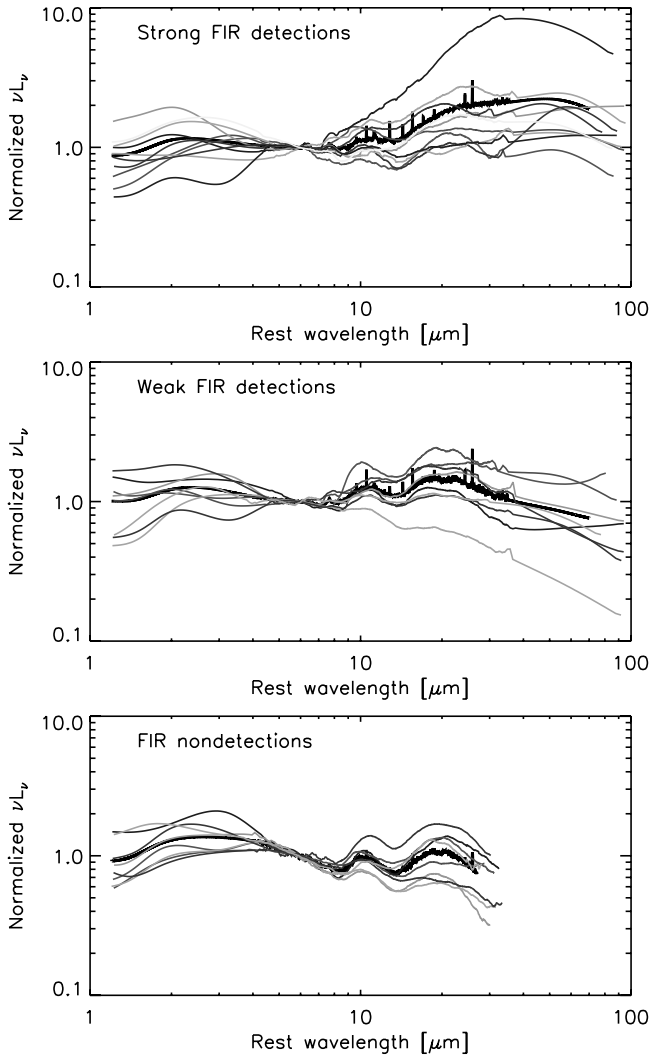

FIG. 4.—SEDs of 10 FIR-strong (*top*), 8 FIR-weak (*middle*), and 8 FIR-undetected (*bottom*) sources. The central ~5–35 μm parts of the curves cover the range of the *Spitzer* IRS spectra, which are shown smoothed here. The short-wavelength part (optical, *J*, *H*, *K*, and *L* photometry) and the long-wavelength *IRAS* or *ISO* data have been joined to the IRS spectra by interpolating splines. The black heavy lines are the mean spectra of the two groups already shown in Fig. 3, and the colored curves show the scatter of individual objects around this mean. All spectra are normalized at 6 μm rest wavelength. [*See the electronic edition of the Journal for a color version of this figure.*]

of all sources. This radiation is thought to be emitted by the central accretion disk and is thus primary. We can directly compare this radiation with several of the IR components, including those suspected to be of starburst origin. In the following we use $L(5100)$ to specify λL_λ at 5100 Å. This quantity is relatively easy to measure and is widely used to derive the broad-line region size and the central BH hole masses in AGNs (e.g., Kaspi et al. 2005).

The correlation of $L(5100)$ with $L(60\ \mu\mathrm{m})$ is shown in Figure 5, where we plot data for all the QUEST QSOs (21 detections and 8 upper limits). The diagram exhibits a very strong correlation over more than 2 orders of magnitude in $L(5100)$, with a slope $\alpha \simeq 0.8$ [$L(60\ \mu\mathrm{m}) \propto L(5100)^\alpha$] for the 60 μm–detected sources. The error on the slope is about 0.16, again using only real detections. Assuming that the upper limits represent real detections, we get a very significant correlation. However, at this stage the result is not very sound, since testing for the correlation of the observed fluxes (i.e., the observed λf_λ at 60 μm rest wavelength vs. λf_λ at 5100 Å rest wavelength) gives a much

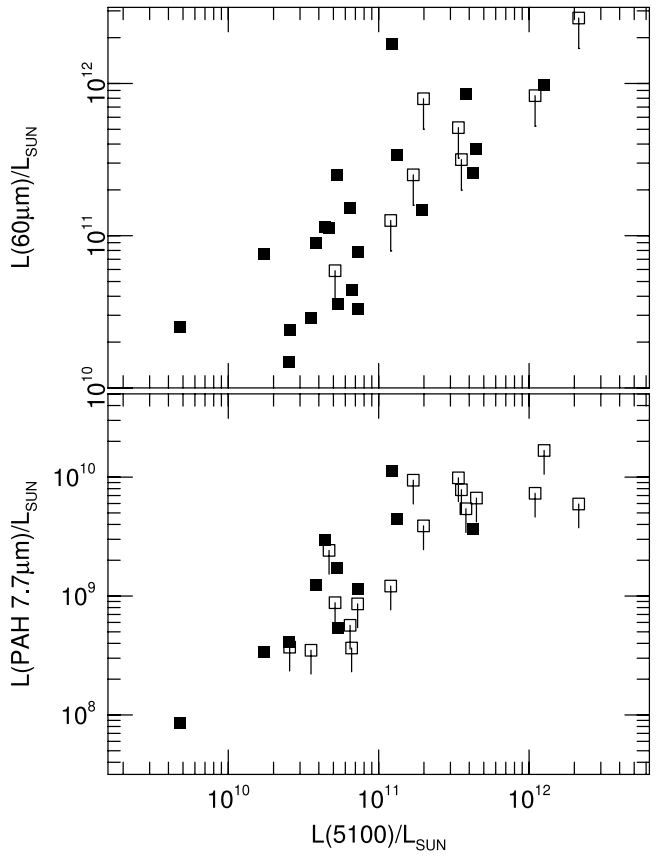

FIG. 5.—*Top*: Correlation of the optical (5100 Å) and FIR (60 μm) continuum luminosities. *Bottom*: L(5100) vs. L(PAH 7.7 μm) showing detections (*filled squares*) and upper limits (*open squares*).

weaker dependence (rank correlation of 98% significance when all sources are included). This is likely the result of the large spread in L(FIR) and L(60 μm) together with the very limited flux range of the sample. A larger sample is required to verify this relationship. Notwithstanding this limitation, we proceed by assuming that the two luminosities are indeed correlated and discuss the implications for AGN physics.

Estimates of the bolometric luminosity, $L_{\rm bol}$, of unreddened AGNs (e.g., Shemmer et al. 2004; Marconi et al. 2004; Netzer & Trakhtenbrot 2007) are 5–10 times larger than they are for L(5100). In this context $L_{\rm bol}$ applies to the primary continuum radiation, and the references noted above suggest that the bolometric correction is probably luminosity dependent. For the luminosity range of the QUEST QSOs, $L_{\rm bol} \sim 7L(5100)$. This issue is crucial to our work, and we need to describe it in more detail.

The multiwavelength multiobject study by R06 followed the Elvis et al. (1994) approach and recommended a large bolometric correction ($\sim$12) relative to L(5100). The number was obtained by integrating over the entire continuum, including the infrared part. According to our definition, there is a clear distinction between the primary and secondary sources of radiation. The former is the result of the accretion disk and its corona (or alternative X-ray–producing mechanism), and the latter is due to reprocessed radiation. The bolometric correction factor of $\sim$7 used here assumes isotropic radiation by the primary source at all wavelengths. Under this assumption, the R06 procedure involves double counting; hence the larger bolometric correction factor obtained by these authors. In our sample L(FIR) is on average very similar to L(5100) (see Fig. 5). Given the above bolometric correction, we find that for QUEST QSOs, L(FIR) is roughly 10%–20% of the (primary) AGN bolometric luminosity.

A similar correlation to the one shown in Figure 5 was also found by Haas et al. (2003) in their study of a large sample of PG QSOs (see Fig. 4 in their paper). That sample contains a small number of sources with optical luminosities that are significantly higher than those considered here. The Haas et al. sources seem to deviate from the almost 1:1 relationship found here, with a hint that the FIR luminosity levels off at around $10^{13}\ L_{\odot}$. [Note that Haas et al. use L_B, which is somewhat different than L(5100) used here.]

We also test the correlation of L(5100) with L(PAH 7.7 μm), which was not available in the Haas et al. (2003) sample. As noted earlier, there are 11 sources with direct L(PAH 7.7 μm) measurements and 17 with upper limits. All are plotted in the bottom part of Figure 5. The diagram suggests a tight correlation between the two properties, with the more optically luminous sources also the ones with larger L(PAH 7.7 μm). This suggestion was not investigated statistically, since the majority of sources do not have direct PAH detections. The strong correlation is not surprising given the correlations of both L(5100) and L(PAH 7.7 μm) with L(FIR) and the fact that most measured upper limits on L(PAH 7.7 μm) are likely to be within a factor of 2–3 of the real L(PAH 7.7 μm) (Paper I). While we are not in a position to test this relationship for sources with $L(5100) > 10^{12}\ L_{\odot}$, we note the tendency of upper limits at the high-L end of the diagram to fall below the relationship seen for the lower luminosities. This is now confirmed by the recent work of Maiolino et al. (2007), who studied much higher luminosity QSOs.

3. DISCUSSION

3.1. *Possible Origins of the FIR Emission*

The present study extends the work of Sanders et al. (1989), Elvis et al. (1994), Kuraszkiewicz et al. (2003), Haas et al. (2003), R06, and others, who studied the IR-SED of various subgroups of AGNs. Many of the spectra used to construct those SEDs are of sources that were either found in X-ray–selected samples (e.g., the sources in Elvis et al. [1994] and Kuraszkiewicz et al. [2003]) or in UV-selected samples (the PG samples of Sanders et al. [1989] and Haas et al. [2003]). Our QUEST sample is very similar to the Sanders et al. (1989) sample and also to the other samples containing UV-selected X-ray–bright QSOs. Two important differences are the small fraction of radio-loud sources in our QUEST sample (5 out of 29 QSOs, compared with about 50% of the sources in Haas et al. [2003]) and the smaller range in optical luminosity (only 2 orders of magnitude). Despite the relatively small luminosity range, the diversity in spectral properties in our sample is large, with a clear distinction between weak and strong FIR sources (Fig. 4). Most important regarding the comparison with earlier works is the greater level of detail over the 6–35 μm range, where the *Spitzer* IRS is clearly superior to previous instruments. In this respect our SEDs are superior to the (much larger number of) broadband R06 SEDs. This improved resolution results in the detections of previously unobserved PAH features (Paper I), in a real correlation between L(PAH 7.7 μm) and L(FIR) in QUEST QSOs, and in a more detailed view of the shape and the strength of several MIR features, such as the silicate bumps centered at around 10 and 18 μm.

A major goal of the present investigation is to isolate the AGN-powered IR spectrum of the QUEST QSOs. This requires an understanding of the origin of the FIR emission and a comparison with theoretical models that predict the expected dust

emission under different conditions. There are a number of such models in the literature, including those of Pier & Krolik (1992; 1993), Granato & Danese (1994), Efstathiou & Rowan-Robinson (1995), Nenkova et al. (2002), and Kuraszkiewicz et al. (2003). They address various possibilities regarding the dust distributions, the orientation of the central torus, and the overall geometry. In general, such models can be divided into two groups: those assuming a continuous gas distribution (all models except those of Nenkova et al.) and those assuming a clumpy dusty medium (Nenkova et al. 2002; see also Elitzur et al. 2004). Examples of fits to observed IR spectra are shown in Kuraszkiewicz et al. (2003), which presents models of the SEDs of three QSOs in Pier & Krolik (1993, see Fig. 5) and Nenkova et al. (2002, e.g., Fig. 3). Key issues in such models are the agreement with the observed NIR-MIR spectrum and the question of whether the FIR emission is due to the same central structure or whether it is produced independently by isolated kiloparsec-scale star-forming regions in the host galaxy.

Kiloparsec-scale luminous star-forming regions have been proposed in several papers as the origin of the FIR radiation in QSOs and in lower luminosity Seyfert galaxies (e.g., Rowan-Robinson 1995; Barthel 2006). Haas et al. (2003) address this possibility in their comprehensive investigation of a sample of 47 PG QSOs, which covers about 3 orders of magnitude in optical continuum luminosity. In particular, they provide estimated dust temperatures, which are required to explain the observed FIR spectrum of all sources. These estimates are based on broadband measurements of the 20–100 μm continuum and suggest a typical dust temperature of 30–50 K for most sources, similar to the range found for nearby ULIRGs by Klaas et al. (2001). According to Haas et al. (2003) the high-redshift highest luminosity sources in the sample exhibit a warmer IR continuum that peaks in the MIR part of the spectrum. In such sources the entire 50–150 μm part of the spectrum is interpreted as the Rayleigh-Jeans tail of an AGN-heated dust component. Haas et al. (2003) further searched for PAH emission in those sources. While they did not have any detections, they commented on the fact that the derived upper limits are consistent with the assumption that the entire FIR luminosity is of starburst origin, except for the few most luminous QSOs in their sample.

Further general support for the likely SF origin of the FIR emission comes from the correlation of radio and infrared properties. According to Haas et al. (2003) the observed L(1.4 GHz)/L(FIR) ratio in radio-quiet QSOs (about 50% of the sources in their sample) is very similar to the ratio observed in starburst galaxies (Condon 1992), where the FIR emission is due to starburst-heated dust, and the radio emission due to supernovae is proportional to the star formation rate. Radio-loud QSOs contain an additional, more powerful radio source that is associated with the compact active core of the AGN. The Condon (1992) relation applied to our sample seems to provide a firm lower limit to the radio emission of all PG quasars. This strengthens the assumption that powerful star formation is taking place in most, and perhaps all, such sources.

Given all these findings, we proceed to discuss two different scenarios. The first involves two separate IR sources: an inner structure that emits the 1–40 μm continuum and a surrounding SF region that emits the FIR continuum and the associated PAH emission features. The second scenario requires only one large dusty structure that produces the entire IR spectrum by absorption and reemission of the primary source radiation at different distances. Along the way we also discuss caveats related to the expected range in L(FIR)/L(PAH).

3.2. *The Intrinsic SED of Type I AGNs*

3.2.1. *Starburst-produced FIR Continuum*

We first consider the possibility that the infrared SED of the QUEST QSOs contains two distinct components: one originating in a dusty central structure and the other in extended SF regions. As shown in Paper I, the QUEST observations are consistent with the assumption that at least one-third and perhaps almost all of the FIR emission is due to starbursts. Given a 100% starburst contribution, we find that the starburst luminosity in our sample is between 1.6×10^{10} and 2.5×10^{12} $L_{\odot}$, and the corresponding (somewhat model-dependent) star formation rate is between about 2 and 300 $M_{\odot}$ yr^{-1}. We caution that the results presented below may not apply outside the luminosity range considered here. Thus, sources such as those observed by Haas et al. (2003), which are an order of magnitude more luminous than the most luminous QUEST QSOs, may contain a different combination of warm AGN-heated and cold starburst-heated dust.

We proceed to produce a template starburst SED that we then subtract from the spectra of all the QUEST QSOs. The best estimate for such a template is the mean spectrum of the 12 starburst-dominated ULIRGs in our QUEST sample that do not show such AGN indicators as strong mid-IR continuum or high-excitation lines like [Ne V] or [O IV] and also do not show strong MIR absorption (the SB-ULIRG group also discussed in Paper I, § 4.1). The detailed properties of those 12 ULIRGs will be discussed in a future paper; here we only use their composite spectrum. This choice is preferable to the use of templates based on observations of nearby starburst galaxies, since these are not only different in their starburst properties but are also subjected to aperture, metallicity, and luminosity effects.

Our starburst-dominated ULIRG template was obtained by normalizing the 12 spectra to have the same 60 μm flux and then taking the mean at every wavelength. The individual spectra show modest spread around the mean for all $\lambda > 5$ μm, which is the part of the spectrum relevant for our analysis. This starburst-dominated ULIRG template was subtracted from the two mean QSO spectra (weak and strong FIR emitters), scaled consistent with the assumption that most of the 50–100 μm emission is due to star formation. The normalization adopted made the long-wavelength part of the residual spectrum, after subtraction (i.e., the part assumed to be the intrinsic AGN SED), consistent with optically thin dust emission. The presence of such an optically thin AGN dust component is also indicated by the silicate emission features. We have used optically thin dust models that were computed for fitting the silicate emission in QUEST QSOs (M. Schweitzer et al. 2007, in preparation). This method dictated the fractional amount of starburst contribution at those wavelengths, albeit with a rather large uncertainty. It resulted in ~87% due to starbursts at 60 μm for the strong FIR case and ~80% for the weak FIR case. Figure 6 shows the two mean QSO spectra before and after this subtraction. The adopted starburst template is consistent with the L(PAH 7.7 μm)-L(FIR) correlation for QSOs (Fig. 4 of Paper I) and the similarity of PAH 7.7 μm/FIR ratios in PG QSOs and star-bursting ULIRGs stated there. The scaling is also independently supported by the absence of PAH residuals in the subtracted spectra of Figure 6. We thus obtain "intrinsic AGN" SEDs for each of the two groups.

The assumption that most of the FIR emission is due to a starburst component results in a clear drop of the computed AGN SED at long wavelengths. While the exact $\lambda > 30$ μm slope depends on the adopted scaling, a clear decay in λF_{λ} beyond 30 μm cannot be avoided without leaving significant PAH residues,

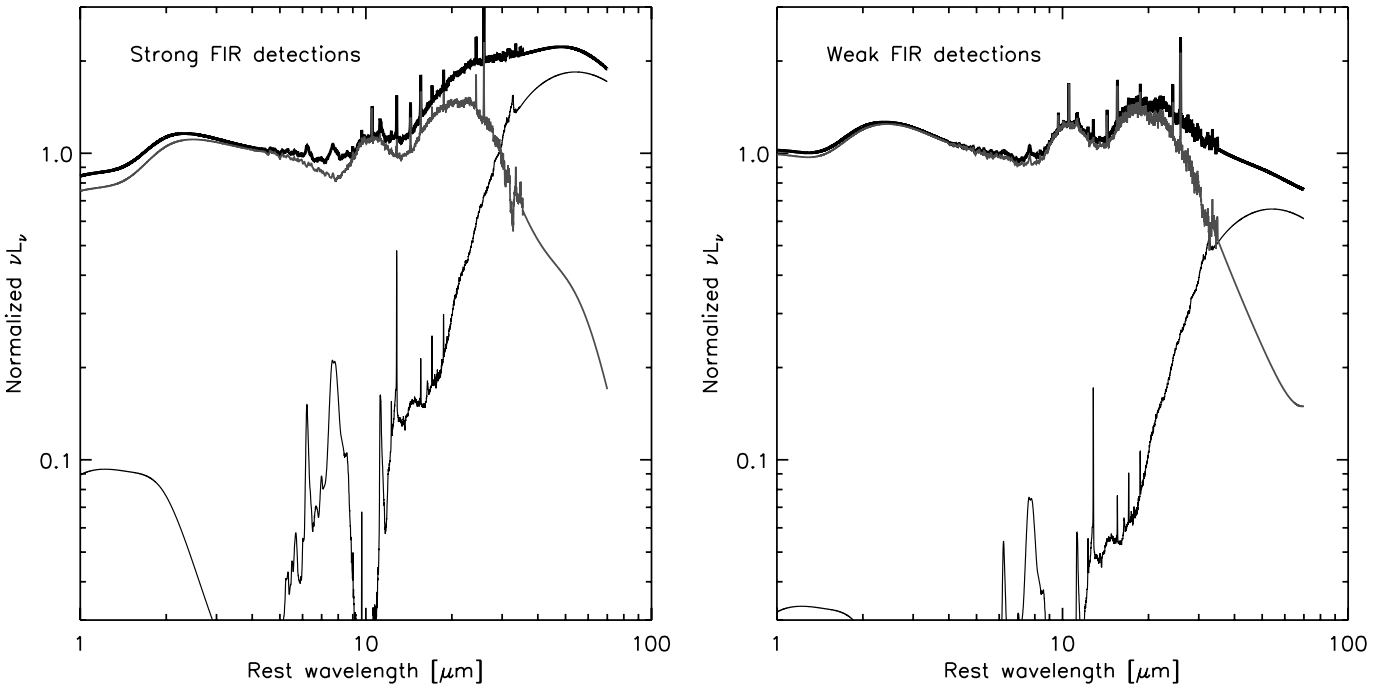

FIG. 6.—Normalized mean SEDs for strong FIR QSOs (*left*, *top curve*) and weak FIR QSOs (*right*, *top curve*). The adjacent red SED curves show "intrinsic" AGN SEDs obtained by the subtraction of the scaled mean starburst (ULIRG) spectrum (*shown in black*) from the mean SEDs. (See text for explanation.) [*See the electronic edition of the Journal for a color version of this figure.*]

which would indicate failure to subtract star formation. In contrast, our intrinsic AGN SEDs show only some [Ne VI] 7.6 μm emission left on top of the continuum in the 6–8 μm region. As is evident from Figures 1 and 6, almost all of our sources and the two median SEDs contain noticeable silicate features that must originate in optically thin regions of dust emission. The inferred long-wavelength drop of our intrinsic AGN SED is consistent with this component, since it suggests a slope that is steeper than a blackbody slope. A flatter SED (in particular for the FIR-strong sources) would require an alternative explanation.

Inspection of Figure 6 reveals a high degree of similarity between the intrinsic AGN SEDs of weak and strong FIR emitters. They both show a relatively flat spectrum in λL_λ with three distinct "bumps": two corresponding to the silicate features at 10 and 18 μm, and a third that is centered at around 3 μm. The average SED of the sources with FIR upper limits is also in agreement with the two mean SEDs over the wavelength range where it is available, and it also shows the same three bumps. Table 2 lists the intrinsic 1–40 μm spectrum of the weak FIR group in normalized flux units.

The short-wavelength feature has been noted in various earlier papers, most recently by Glikman et al. (2006; see references therein to earlier work), who could only observe the short-wavelength side of the feature and modeled it as a combination of a nonthermal power law and a 1260 K blackbody. It extends from below 1 μm (the "1 μm inflection" in R06) to about 5–8 μm and is better seen in our new SEDs because of the much clearer view of the 5–10 μm part of the spectra, where the long-wavelength upturn of this feature is included in the *Spitzer* spectral range. We interpret this feature as the signature of the hottest dust in the AGN inner structure, at a temperature of 1000–1500 K. Obviously, a realistic torus will radiate over a range of temperatures. We also caution that there is a relatively wide range and a large scatter among the individual sources of our sample in this part of the spectrum and some of the data (e.g., the *L*-band photometry) are incomplete. Given these qualifications, the difference between the two intrinsic SEDs presented here is surprisingly small.

In summary, the SF-dominated scenario for the FIR implies similar AGN SEDs for all sources, showing three distinct NIR-MIR humps and very similar long-wavelength ($\lambda > 20$ μm) slopes. Such a slope is consistent with the observed silicate features and can be attributed to the absence of large amounts of AGN-heated dust with temperatures below about 200 K.

3.2.2. *AGN-produced FIR Continuum*

An alternative view is that direct AGN heating, followed by reradiation of cool distant dust, is the origin of a large fraction of the observed FIR emission. Such a scenario has been discussed in several earlier papers, including Sanders et al. (1989) and Haas et al. (2003). Successful models of this type must explain the required range of dust temperatures, as well as the FIR luminosity and the strength of the PAH emission. In this case the differences between strong-FIR and weak-FIR emitters reflect a range in dust temperature. For sources of similar primary luminosity, differing SEDs imply different dimensions and/or geometry of the inner dusty structure.

For the QSOs under study, the FIR luminosity is comparable to $L(5100)$, which in turn represents some 15% of the bolometric luminosity (§ 2.4) [the ratio has a weak dependence on $L(5100)$ that we ignore here]. Thus, $L_{12} \simeq 7L_{12}(\mathrm{FIR})$, where L_{12} and $L_{12}(\mathrm{FIR})$ are the bolometric (primary) and FIR luminosities in units of 10^{12} $L_\odot$, respectively. In general, continuous dust distribution models, such as those published by Pier & Krolik (1993), would fail to produce such a large FIR luminosity, since the assumed torus geometries result in a strong attenuation of the central source radiation at large distances. A somewhat different geometry, involving a flaring or warped disk, can solve the FIR energy budget problem, but it introduces a related problem of extremely large dimensions. This case is easily understood if

we consider the case of a dusty region that is fully exposed to the central source of radiation. In such gas (e.g., Phinney 1989)

$$T_{\rm dust} \simeq 1500 r_{\rm pc}^{-t} L_{12}^{1/4}\ {\rm K}, \quad (1)$$

where $r_{\rm pc}$ is the distance from the central source in parsecs and $t = 2/(4+s)$. For optically thick dust $s = 0$, and for other cases it describes the frequency variation of the dust cross section ($\sigma_\lambda \propto \lambda^{-s}$). For most cases of interest $s = 1$–2.

The present scenario suggests that the 50–100 μm emission of the QUEST QSOs is mostly from dust with $T_{\rm dust} \simeq 40$–65 K. For a typical low-luminosity source in our sample $L_{12} \simeq 0.2$, which for the optically thick case with $T_{\rm dust} = 50$ K gives $r \simeq 0.4$ kpc. For optically thin dust with $s = 1.5$ we get $r \simeq 1.7$ kpc. The derived dimensions for the highest luminosity QUEST QSOs, with $L_{12} \sim 17$, are an order or magnitude or more larger.

Given the inferred dimensions and the fraction of the bolometric luminosity absorbed by the dust, we find that the distant dusty gas in the most luminous QUEST QSOs must rise to a height of at least 0.6 kpc, and perhaps much higher, above the galactic plane. Such a huge structure must have unusual dynamical consequences and is not consistent with a stable, relaxed system. The limitations are probably less severe in interacting systems, where warped galactic disks may be involved. The solid angle in this case can be considerably larger, especially during the later phases of the merger.

The clumpy models of Nenkova et al. (2002) come closer to the observed dimensions, since in those cases nearby clumps can contribute to the IR emission from their hot (illuminated) as well as their cold (backside) faces. In such cases the dimensions can be smaller, and the only firm lower limit on $r_{\rm pc}$ is obtained from simple blackbody considerations. For a partially filled radiating spherical surface of solid angle Ω, $r_{\rm pc} \simeq 2.7 \times 10^6 T_{\rm dust}^{-2} L_{12}^{1/2}({\rm FIR})\Omega^{-1/2}$. Assuming $T = 50$ K and guessing $\Omega/4\pi \simeq 0.2$, we get in this case, for the most luminous QUEST QSOs, a radius of about 1 kpc.

The critical challenge for the cool AGN-heated dust scenario is the presence of strong PAH emission features in many of our QSOs and in the average SEDs, which are naturally associated with the FIR emission if the latter is assumed to be due to star formation. This difficulty arises independently of the assumed dimension of the cool dust region. However, the exact amount of starburst-produced FIR emission requires more discussion. In particular, the specific $L({\rm FIR})/L({\rm PAH})$ ratio observed in star-forming ULIRGs and adopted here naturally leads to the scenario of starburst-dominated FIR emission discussed in the previous section. However, this ratio is known to depend on the conditions in the ISM and in some cases can be significantly lower than the one assumed here. This is known to be the case in quiescent "cirrus-type" hosts. In the extreme case of $\sim$10 times lower $L({\rm FIR})/L({\rm PAH})$ ratio (known for some quiescent disks) a flat or a rising intrinsic AGN continuum out to FIR wavelengths remains possible. Cirrus-type conditions cannot be excluded for the low PAH and FIR luminosity members of our sample, which overlap with luminosities of quiescent galaxies (Paper I), but they become progressively unlikely at high star-forming luminosities in the LIRG and ULIRG regime. More support for a ULIRG-like FIR-to-PAH ratio in QSO hosts is given by the recent finding of a ULIRG-like ratio in the $\sim$5 times more luminous Cloverleaf QSO (Lutz et al. 2007), where the observed $L({\rm PAH})$ is much higher than in known quiescent disks.

Considerations of cirrus emission add to the uncertainty on the $\lambda > 30$ μm slope of the intrinsic AGN SED derived in the previous section. They clearly allow for the possibility of a flatter long-wavelength slope for the QSOs with lower $L({\rm PAH})$ and $L({\rm FIR})$. Most of these sources belong to our FIR-weak group with global SEDs, for which the slope already begins to fall gently at longer wavelengths. Thus, a declining FIR component must also be present in the intrinsic AGN SED, even if $L({\rm FIR})/L({\rm PAH})$ is smaller than the one assumed here. As for those sources with larger $L({\rm PAH})$ and $L({\rm FIR})$, the assumed ULIRG-like ratio is favored because of the similar luminosity to the QUEST ULIRGs. Here again, the intrinsic AGN SED must be falling at long wavelengths, although with a considerable uncertainty on the slope.

To summarize, the assumption of AGN-dominated FIR emission requires a solution to both the PAH and dimension problems. It would also require an explanation for the almost identical ratios between $L({\rm FIR})$ and $L({\rm PAH}\ 7.7\ \mu{\rm m})$ observed in our QUEST QSOs and in ULIRGs (Paper I). We therefore consider the assumption of a starburst-dominated FIR emission to be more plausible for the PG QSOs discussed here. For QSOs with a larger ratio of AGN to host luminosity, the intrinsic AGN SED may dominate the emission out to longer wavelengths.

3.3. *The AGN-Starburst Connection at Low and High Redshift*

The observations shown in Figure 5 clearly suggest significant correlations between the primary AGN continuum and the starburst-produced emission (given our preferred explanation for the origin of the FIR emission). This conclusion was already pointed out in Paper I, in which similar correlations between, e.g., $L(6\ \mu{\rm m})$ and $L(60\ \mu{\rm m})$ were shown. This relation is of considerable theoretical interest, since current galaxy and BH evolution models do not predict a specific trend and only describe a general evolutionary relationship that is not necessarily coeval. Models such as these based on detailed numerical simulations (e.g., Hopkins et al. 2006; Volonteri et al. 2006; Granato et al. 2004) calculate the star formation rate and the BH growth rates as functions of cosmic time, yet they definitely allow a time lag between the end of star formation and the commencement of black hole activity. Our observations of the QUEST sample do not require such a delay at redshifts 0.1–0.3. The sample may not represent all AGNs, but it gives a fair representation of unobscured sources at those redshifts. Our findings may indicate that enhanced SF activity, when present, includes the very central part of the galaxy. Thus, some of the starburst-produced gas can find its way to the vicinity of the BH on a timescale that is short compared to the lifetime of the global, galactic-scale starburst activity. More complicated scenarios including the obscured and unobscured phases of a certain source (e.g., Hopkins et al. 2006) are also possible.

A similar phenomenon may well be occurring at redshifts much larger than 0.3. Deep submillimeter and millimeter photometry has led to the detection of rest-frame submillimeter and far-infrared dust emission from radio-quiet quasars at redshifts up to 6.42 (e.g., Omont et al. 2001; Isaak et al. 2002; Bertoldi et al. 2003). Indirect arguments, such as CO measurements, have been used to suggest that this emission is powered by star formation, implying that these quasars coexist with extremely powerful $\gtrsim 10^{13}\ L_\odot$ starbursts. If the relation of PAH to FIR emission in these QSOs is similar to the one in ULIRGs, detection of PAH on top of a strong continuum may be within the reach of *Spitzer* spectroscopy. PAH emission from similar luminosity SMGs has been shown to be detectable, e.g., Lutz et al. (2005). Clearly the extrapolation of the relationships found here to higher redshift, higher luminosity AGNs depends on the ability to detect PAH features in such sources. There are already some interesting upper limits in several extremely luminous QSOs (Maiolino

et al. 2007), as well as one real detection in a high-redshift high-luminosity QSO with a strong millimeter flux (Lutz et al. 2007).

Having measured the $L(5100)$-$L(\mathrm{FIR})$ relationship, we can estimate the relative growth rate of the central BH and the galactic bulge, assuming all the observed star-forming activity contributes to the growth of the bulge. For the QUEST QSOs, $L(\mathrm{FIR})/L_{\mathrm{bol}} \simeq 0.15$. Assuming a BH accretion efficiency η, we can convert the (primary) bolometric luminosity to BH mass growth rate and the observed FIR luminosity to star formation rate. This gives $g(\mathrm{bulge})/g(\mathrm{BH}) \sim 20(\eta/0.1)$, where g stands for growth rate. This is more than an order of magnitude smaller than that required to explain the locally observed bulge and BH mass ratio under the assumption of a similar duration for the two phenomena. Thus, the numbers presented here may indicate that the AGN activity phase is, on average, an order of magnitude shorter than the star formation phase. It would be interesting to carry out a similar analysis for higher redshift, higher luminosity AGNs. For example, Steidel et al. (2002) suggest AGN fractions of about 3% in $z \sim 3$ UV-selected samples, not very different from what was found here.

4. CONCLUSIONS

The main conclusion of the present work, and of Paper I, is that most and perhaps all of the FIR luminosity of the QUEST QSOs is due to starburst activity. This conclusion is based mostly on the tight correlation between the luminosity of the PAH 7.7 μm feature and the FIR luminosity. As explained in § 3, there are alternative relationships for $L(\mathrm{FIR})/L(\mathrm{PAH})$ that are different from the ones used here, but these we consider inapplicable to the objects in question. While there are clear PAH 7.7 μm detections in only 11 of the sources studied here, most of the derived upper limits, as well as the composite spectrum of all sources *not showing* clear PAH emission, are consistent with this assumption (Paper I). In this scenario the starburst luminosity in our sample is between 1.6×10^{10} and $2.5 \times 10^{12}\ L_{\odot}$, corresponding to star formation rates of about 2 and 300 $M_{\odot}\ \mathrm{yr}^{-1}$. The upper luminosity range is close to the luminosity of the most luminous starburst-dominated ULIRGs in our sample.

The assumption that most of FIR luminosity is due to starburst activity allows us to estimate the minimum temperature of the AGN-heated dust in the central dusty structures of our QSOs. This temperature is of order 200 K. The inferred maximum dimensions of the torus in the simplest, continuous gas distribution case is of order $100L_{12}^{1/2}$ pc, in reasonable agreement with all available observations.

Finally, our work shows that observed AGN SEDs can be misleading, showing shapes that are quite different from the intrinsic SED. We suggest that future AGN models that try to reproduce the NIR-FIR spectrum of type I sources use the results presented in Figure 6 and Table 2 as a more realistic representation of the intrinsic AGN spectrum.

We thank Todd Boroson for kindly allowing us to use his optical data for PG quasars. We thank Amiel Sternberg for discussions and comments on the manuscript. Funding for this work has been provided by the Israel Science Foundation grant 232/03. S. V., D. S. R., and D. C. K. were supported in part by NASA contract 1263752 issued by the Jet Propulsion Laboratory, California Institute of Technology. H. N. acknowledges a Humboldt Foundation prize and thanks the host institution, MPE Garching, where most of this work was performed.

REFERENCES

Barthel, P. D. 2006, A&A, 458, 107
Bertoldi, F., Carilli, C. L., Cox, P., Fan, X., Strauss, M. A., Beelen, A., Omont, A., & Zylka, R. 2003, A&A, 406, L55
Boroson, T. A., & Green, R. F. 1992, ApJS, 80, 109
Condon, J. J. 1992, ARA&A, 30, 575
Efstathiou, A., & Rowan-Robinson, M. 1995, MNRAS, 273, 649
Elitzur, M., Nenkova, M., & Ivezić, Z. 2004, in ASP Conf. Ser. 320, The Neutral ISM in Starburst Galaxies (San Francisco: ASP), 242
Elvis, M., et al. 1994, ApJS, 95, 1
Glikman, E., Helfand, D. J., & White, R. L. 2006, ApJ, 640, 579
Granato, G. L., & Danese, L. 1994, MNRAS, 268, 235
Granato, G. L., de Zotti, G., Silva, L., Bressan, A., & Danese, L. 2004, ApJ, 600, 580
Guyon, O., Sanders, D. B., & Stockton, A. 2006, ApJS, 166, 89
Haas, M., et al. 2003, A&A, 402, 87
Hatziminaoglou, E., et al. 2005, AJ, 129, 1198
Hopkins, P. F., Hernquist, L., Cox, T. J., Di Matteo, T., Robertson, B., & Springel, V. 2006, ApJS, 163, 1
Hyland, A. R., & Allen, D. A. 1982, MNRAS, 199, 943
Isaak, K. G., Priddey, R. S., McMahon, R. G., Omont, A., Peroux, C., Sharp, R. G., & Withington, S. 2002, MNRAS, 329, 149
Jarrett, T. H., Chester, T., Cutri, R., Schneider, S., Skrutskie, M., & Huchra, J. P. 2000, AJ, 119, 2498
Kaspi, S., Maoz, D., Netzer, H., Peterson, B. M., Vestergaard, M., & Jannuzi, B. T. 2005, ApJ, 629, 61
Klaas, U., et al. 2001, A&A, 379, 823
Kuraszkiewicz, J. K., et al. 2003, ApJ, 590, 128
Lacy, M., et al. 2004, ApJS, 154, 166
Lutz, D., Valiante, E., Sturm, E., Genzel, R., Tacconi, L. J., Lehnert, M. D., Sternberg, A., & Baker, A. J. 2005, ApJ, 625, L83
Lutz, D., et al. 2007, ApJ, 661, L25
Maiolino, R., Shemmer, O., Imanishi, M., Netzer, H., Oliva, E., Lutz, D., & Sturm, E. 2007, A&A, 468, 979
Marconi, A., Risaliti, G., Gilli, R., Hunt, L. K., Maiolino, R., & Salvati, M. 2004, MNRAS, 351, 169
McAlary, C. W., McLaren, R. A., McGonegal, R. J., & Maza, J. 1983, ApJS, 52, 341
Nenkova, M., Ivezić, Ž., & Elitzur, M. 2002, ApJ, 570, L9
Netzer, H., & Trakhtenbrot, B. 2007, ApJ, 654, 754
Neugebauer, G., Green, R. F., Matthews, K., Schmidt, M., Soifer, B. T., & Bennett, J. 1987, ApJS, 63, 615
Omont, A., Cox, P., Bertoldi, F., McMahon, R. G., Carilli, C., & Isaak, K. G. 2001, A&A, 374, 371
Pier, E. A., & Krolik, J. H. 1992, ApJ, 399, L23
———. 1993, ApJ, 418, 673
Phinney, E. S. 1989, in Theory of Accretion Disks, ed. F. Meyer (Dordrecht: Kluwer), 457
Richards, G. T., et al. 2006, ApJS, 166, 470
Rowan-Robinson, M. 1995, MNRAS, 272, 737
Sanders, D. B., Phinney, E. S., Neugebauer, G., Soifer, B. T., & Matthews, K. 1989, ApJ, 347, 29
Schweitzer, M., et al. 2006, ApJ, 649, 79 (Paper I)
Scott, J. E., Kriss, G. A., Brotherton, M., Green, R. F., Hutchings, J., Shull, J. W., & Zheng, W. 2004, ApJ, 615, 135
Shemmer, O., Netzer, H., Maiolino, R., Oliva, E., Croom, S., Corbett, E., & di Fabrizio, L. 2004, ApJ, 614, 547
Steidel, C., et al. 2002, ApJ, 576, 653
Trammell, G. B., Vanden Berk, D. E., Schneider, D. P., Richards, G. T., Hall, P. B., Anderson, S. F., & Brinkmann, J. 2007, AJ, 133, 1780
Volonteri, M., Salvaterra, R., & Haardt, F. 2006, MNRAS, 373, 121